Available online at www.sciencedirect.com
ScienceDirect
Journal of Solid State Chemistry 180 (2007) 2958–2972
JOURNAL OF SOLID STATE CHEMISTRY
www.elsevier.com/locate/jssc

Synthesis and physicochemical properties of Zr-MCM-41 mesoporous molecular sieves and $Pt/H_3PW_{12}O_{40}$/Zr-MCM-41 catalysts

L.F. Chen[a,*], J.A. Wang[a], L.E. Noreña[b], J. Aguilar[b], J. Navarrete[c], P. Salas[c], J.A. Montoya[c], P. Del Ángel[c]

[a]*Escuela Superior de Ingeniería Química e Industrias Extractivas, Instituto Politécnico Nacional, Col. Zacatenco, 07738 México D.F., México*
[b]*Departamento de Ciencias Básicas, Universidad Autónoma Metropolitana-A, Av. San Pablo No. 180, 02200 México D.F., México*
[c]*Instituto Mexicano del Petróleo, Programa de Ingeniería Molecular, Eje Central Lázaro Cárdenas No. 152, 07730 México D.F., México*

Received 20 June 2007; received in revised form 7 August 2007; accepted 15 August 2007
Available online 6 September 2007

Abstract

For the first time, modifications of the surface and framework of Si-MCM-41 by depositing a heteropolyacid on the surface and by introducing foreign Zr^{4+} ions into the framework are investigated. The Zr-modified Si-MCM-41 mesoporous materials (hereafter referred as WSZ*n*, $n = Si/Zr = 25, 15, 8, 4$) were synthesized through a surfactant-templated preparation approach, using low-cost fumed silica as the Si precursor. After impregnation with 25 wt% of $H_3PW_{12}O_{40}$, the surface Brönsted acidity of the $Pt/H_3PW_{12}O_{40}$/WSZ*n* catalysts was greatly enhanced by 2–10 times relative to the bare WSZ*n* support. Two kinds of supported heteropolyacids were formed: (i) bulk-like heteropolyacid crystals with unchanged *Keggin* structures, and (ii) highly dispersed heteropolyacid with distorted *Keggin* units. The formation of various kinds of heteropolyacid structures is closely related to the interaction between the heteropolyanions and the hydroxyl groups in the host support.

Keywords: Zr-MCM-41; Mesoporous molecular sieves; Catalyst; Heteropolyacids; *Keggin* structure; Acidity

1. Introduction

It has been proved that Si-MCM-41 lacks Brönsted acid sites and exhibits only weak hydrogen-bonded type of sites [1–3]. In the case of acid-catalyzed reactions such as the isomerization of hydrocarbons, where catalysts having both an acid functionality as well as a metal (Pt) are required, when the Si-MCM-41 is used as catalyst or catalyst support, surface Brönsted acid sites of Si-MCM-41 solid need to be created and the acid strength must be enhanced.

The acidity of Si-MCM-41 can be increased by surface modification. By introducing some strong acid species like sulfate ions [4], sulfated zirconia [5] or heteropolyacids with *Keggin* structure [6,7], either on the surface or the inner channels of Si-MCM-41, not only the Brönsted acid sites can be created but also the acid strength can be significantly improved.

The incorporation of foreign ions into the Si-MCM-41 framework for promoting surface acidity is another interesting route. When Si ions in the Si-MCM-41 framework are partially substituted by other ions, such as Al^{3+}, Fe^{3+}, Ti^{4+}, Ga^{3+} and V^{5+}, a variety of framework-modified mesoporous materials with larger surface, modified thermal stability and enhanced surface acidity may be obtained [8–15]. Because of the importance of Zr-based nanomaterials in acid-catalyzed reactions [16–19], it has been our interest to use zirconium ions to partially replace Si ions in the Si-MCM-41 framework, in order to obtain Zr-containing mesostructured solids. Usually, the zirconium ions in mesostructured materials can be accessible to reactants because the majority of them are located on the surface of the pore walls, due to their trend to adopt high coordination numbers [20,21].

ZrO_2–SiO_2 mesoporous materials can be synthesized by either conventional coprecipitation or sol–gel technique

*Corresponding author. Fax: +52 55 55862728.
E-mail address: chenlf2001@yahoo.com (L.F. Chen).

0022-4596/$ - see front matter © 2007 Elsevier Inc. All rights reserved.
doi:10.1016/j.jssc.2007.08.023

using alkoxides as reaction precursors [22,23]. Unfortunately, the low surface area (less than 200 m^2/g) or the high cost of these synthetic approaches for obtaining ZrO_2–SiO_2 materials represent a serious drawback against classical acidic oxides used as supports. Differing from these two traditional synthetic approaches, recently, Wang et al. [24] reported a method by surface grafting tetraneopentyl zirconium on the Si-MCM-41, indeed, the surface acidity of the resultant solids was enhanced; however, the grafting operation was carried out in a vacuum condition and is thus rather complex. Tarafdar et al. [25] reported a sol–gel method in basic conditions by using inexpensive zirconia and silica sources to obtain a mesocomposite with high zirconia content showing both Lewis and Brönsted acidity. However, these mesocomposites have a low porosity, less than 0.4 ml/g. In our previous work [26], by doubly doping Si-MCM-41 by introducing Zr^{4+} into the framework and *in situ* sulfation of the surface, a long-range ordered Zr-containing MCM-41 mesostructure with enhanced thermal stability was obtained, with a surface area larger than 600 m^2/g and a pore volume higher than 0.7 ml/g; unfortunately, the Brönsted acidity of the resultant solids was not noticeably promoted. Therefore, the combination of a regular mesoporous structure and an enhanced surface acidity induced by the presence of zirconium is of particular interest and challenging.

In the present work, modifications of the surface and framework of Si-MCM-41 by depositing the $H_3PW_{12}O_{40}$ heteropolyacid (referred as HPW) on the surface and by introducing foreign Zr^{4+} ions into the framework using a cationic surfactant-templated preparation method are investigated. The synthesis, the structural characteristics and the determination of the surface acidity of a series of Zr-modified mesoporous materials, with enhanced acidity and modified structural regularity are reported. The surface dehydroxylation process and the surfactant template interaction with and removal from the solid, were monitored by the *in situ* Fourier-transform infrared (FTIR) spectroscopy technique. The textural properties including surface area, average pore diameter and pore size distribution, were measured by low temperature N_2-physisorption isotherms. The crystalline structures of the resultant solids were studied by X-ray diffraction (XRD), UV–visible spectroscopy, solid-state ^{29}Si and ^{31}P MAS-NMR and high-resolution transmission electron microscopy (TEM) techniques. Finally, the surface acidity of the bare support and the Pt/HPW/WSZn catalysts were analyzed by *in situ* FTIR spectroscopy of pyridine adsorption at various temperatures.

2. Experimental

2.1. Synthesis of the WSZn (n = Si/Zr = 25, 15, 8, 4) samples

The 0.6 g of fumed silica were added into 5.4 g (40 wt%) of tetrabutylammonium hydroxide (TBAOH) aqueous solution with vigorous stirring for 5 min to form a transparent and uniform gel. Then 12 g of cetyltrimethylammonium chloride (CTACl) (25 wt% solution in water) were added into the above gel with agitation. Afterwards, 1 g of fumed silica was immediately added into the above mixture. The following step is to add a given amount of zirconium-*n*-propoxide (70% in propanol) with vigorous stirring for 15 min; the amount of zirconium-*n*-propoxide depends on the Si/Zr molar ratio. For example, to obtain a solid with a molar ratio of Si/Zr = 15, 0.77 ml of zirconium-*n*-propoxide were added. The resultant gel was loaded into a stoppered Teflon bottle without stirring and kept at 100 °C for 48 h. After cooling to room temperature, the resulting solid product was recovered by filtration and washed extensively with 500 ml of deionized water for 4 times. The white solid obtained was dried in air at 80 °C for 24 h. Finally, the resultant material was calcined at 600 °C for 6 h in air with a flow rate of 60 ml/min. By using the same method, several other samples with different Si/Zr molar ratios (Si/Zr = 25, 8 and 4) were prepared. Hereafter, the solids prepared with this method will be referred to as WSZ*n* (n = Si/Zr = 25, 15, 8 and 4).

2.2. Synthesis of the Pt/HPW/WSZn catalysts

The 1 wt%Pt/25 wt%HPW/Zr-MCM-41 catalysts were prepared by a two-step impregnation method. The Zr-MCM-41 samples were firstly impregnated with 20 ml of a solution containing a given amount of $H_3PW_{12}O_{40}$ in methanol. The solvent was removed at 40 °C in a rotary evaporator until dryness. Afterwards, the 25 wt% HPW/Zr-MCM-41 solids were impregnated with 20 ml of a solution containing H_2PtCl_6 in water. The solvent was evaporated at 80 °C in a rotary evaporator until a dried material with 1 wt% Pt was obtained. The amount of $H_3PW_{12}O_{40}$ and H_2PtCl_6 used depended upon the amount of the support. The dried materials or catalysts were then calcined at 300 °C in air for 2 h.

2.3. Characterization

2.3.1. X-ray diffraction analysis

The low-angle XRD patterns of the samples were measured in a D-500 SIEMENS diffractometer with a graphite secondary beam monochromator to obtain a monochromatic Cu$K\alpha_1$ radiation; the evaluation of the diffractograms was made by DIFFRAC/AT software. The scanning was made from 1.5° to 10° with a 2θ step size of 0.02 and a step time of 2 s. In all the cases, the generator was operated at 40 kV and 30 mA. In order to avoid the problem of illuminated area at low 2θ angle, all the samples were measured using the same sample holder. In this way the hexagonal reflection (100) positions as well as the intensities are directly comparative. Position correction was made using the NIST standard reference material 675.

2.3.2. Measurement of N_2 adsorption–desorption isotherms

The specific surface area, pore volume and pore size distribution of the samples were measured with a Digisorb 2600 equipment by low temperature N_2 adsorption–desorption isotherms. Before the measurement, the sample was evacuated at 350 °C. The surface area was computed from these isotherms by using the multi-point Brunauer–Emmett–Teller (BET) method based on the adsorption data in the partial pressure P/P_o range from 0.01 to 0.2. The value of 0.1620 nm^2 was taken for the cross-section of the physically adsorbed N_2 molecule. The mesopore volume was determined from the N_2 adsorbed at a $P/P_o = 0.4$. The pore diameter and pore volume were determined by using the BJH method. In all cases, correlation coefficients above 0.999 were obtained.

2.3.3. Fourier transform infrared (FTIR) spectroscopy

The surface dehydroxylation and removal of the residual surfactant from the dried samples were followed by using the *in situ* FTIR spectroscopic technique on a Nicolet Magna-IR 550 spectrometer with a 4 cm^{-1} resolution and 128 scans in the mid-IR region 400–4000 cm^{-1}. The sample was ground with KBr and pressed into a thin wafer that was placed inside the IR cell, which was linked with a vacuum and heating system. The sample could be exposed to various gaseous environments under various pressures at temperatures not exceeding 400 °C. The sample was degassed at a desired temperature and then the spectrum was recorded. The *in situ* FTIR spectra were recorded at 25, 100, 200, 300 and 400 °C.

2.3.4. Magic angle spinning nuclear magnetic resonance (MAS-NMR)

Solid-state ^{31}P and ^{29}Si MAS-NMR spectra were recorded on a Bruker 400 MHz spectrometer at room temperature at a frequency of 79.49 MHz. A magic angle spinning rate of 7.5 kHz was employed, sending pulses at 90 s intervals and employing 4 mm zirconia rotors. The number of accumulations was 500. All the measurements were carried out at room temperature under Ar atmosphere for direct quantification. To protect the solid samples from moisture, before and after measurements, the samples were stored in a vacuum oven. Air was used as drive gas in order to obtain as much benefit as possible from O_2 paramagnetic relaxation. The accuracy of the chemical shift determination was within ± 0.1 ppm. For the ^{31}P analysis, 85% H_3PO_4 solution (0 ppm) was used as standard reference to obtain the chemical shift, for the ^{29}Si analysis, tetramethylsilane was used as chemical shift standard (0 ppm); the spectral deconvolution was performed with the Unity spectrometer software and was done in an unconstrained manner, assuming Gaussian line shapes.

2.3.5. High-resolution transmission electron microscopy

High-resolution electron microscopy images of the mesoporous materials and catalysts were carried out with a JEOL 4000 EX electron microscope equipped with a pole piece with a spherical aberration coefficient of $C_s = 1.00$ mm. The powder samples were grounded softly in an agate mortar and dispersed in isopropyl alcohol in an ultrasonic bath for several minutes. A few drops were then deposited on 200 mesh copper grids covered with a holey carbon film. The electron micrographs were recorded in electron negative films and in a digital PC system attached to the electron microscope. The particle size distribution was evaluated from several micrographs taken from the same sample. The particle size was calculated using the equation $d = \sum n_i di / \sum n_i$, where n_i is the number of particles with diameter d_i and $\sum n_i$ is the number of particles used to build the size distribution.

2.3.6. Ultraviolet–visible spectroscopic analysis (UV–vis)

The UV–vis diffuse reflectance spectra of the samples were collected on a Varian Cary 1G UV–visible spectrometer at room temperature. All the samples used for analysis were calcined at 600 °C. Before the experiment, the samples were pre-treated at 300 °C for 2 h. Scan control conditions: average time: 0.10 s; data interval 1.00 nm; scan rate: 600 nm/min; mode: absorption; wavelength range: 190–900 nm.

2.3.7. FTIR spectroscopy of pyridine adsorption

To evaluate and analyze the strength and type of the acid sites, pyridine adsorption on the samples was performed on a 170-SX FTIR spectrometer in the temperature range between 25 and 400 °C. Before pyridine adsorption, the samples were heated to 400 °C in a vacuum, and then cooled to room temperature. Afterwards, the solid wafer was exposed to pyridine, by breaking, inside the spectrometer cell, a capillary containing 50 μl of liquid pyridine. The IR spectra were recorded at various conditions by increasing the cell temperature from 25 to 400 °C. The number of Brönsted and Lewis acid sites was calculated according to the integral area of the bands at 1540 and 1450 cm^{-1}, respectively.

2.3.8. Electron dispersive spectroscopic (EDS) analysis

The morphological features of the samples were also studied from electron micrographs obtained with a Philips XL 30 ESEM scanning electron microscope; the powder samples were deposited directly on a sample holder covered with a conductive adhesive tape. The analytical electron microscopy observations were carried out with an energy-dispersive X-ray analysis (EDAX) system attached to the scanning electron microscope which was operated at 25 kV. The determination of the chemical composition was based on the average analytical data of individual particles.

3. Results and discussion

3.1. The WSZn (n = Si/Zr = 25, 15, 8, 4) supports

3.1.1. Surface characterization by FTIR-in situ technique

Figs. 1–4 show a set of FTIR-*in situ* spectra of the as-prepared WSZ*n* (n = Si/Zr = 25, 15, 8 and 4) samples

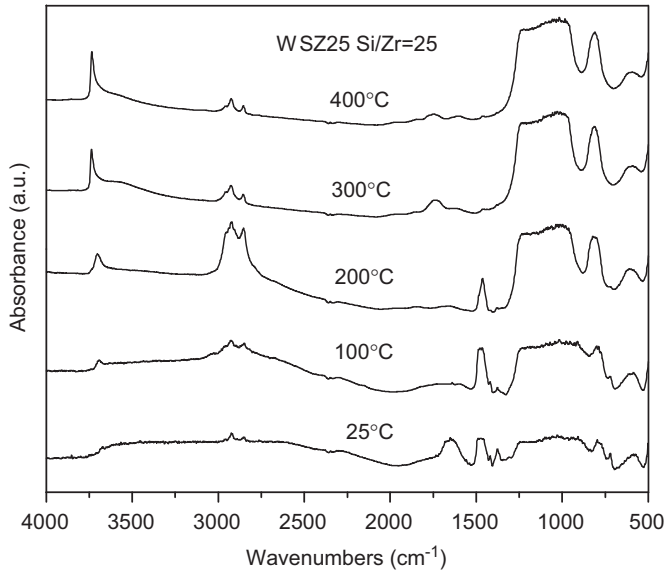

Fig. 1. A set of FTIR-*in situ* spectra of the sample Si/Zr = 25 at various temperatures.

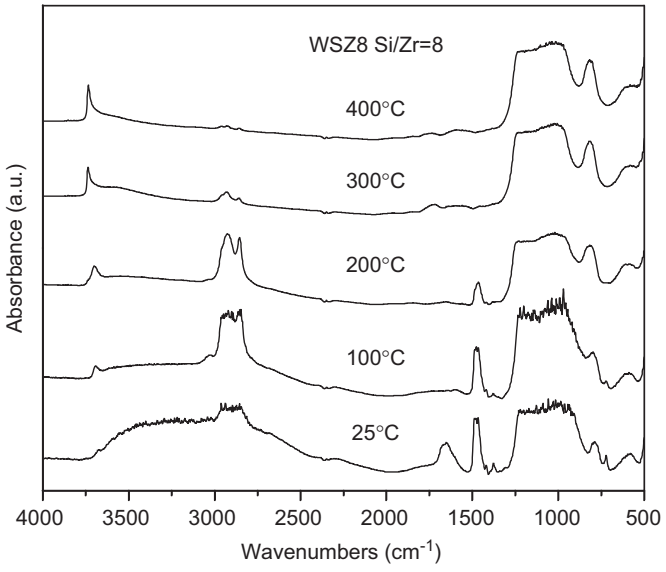

Fig. 3. A set of FTIR-*in situ* spectra of the sample Si/Zr = 8 at various temperatures.

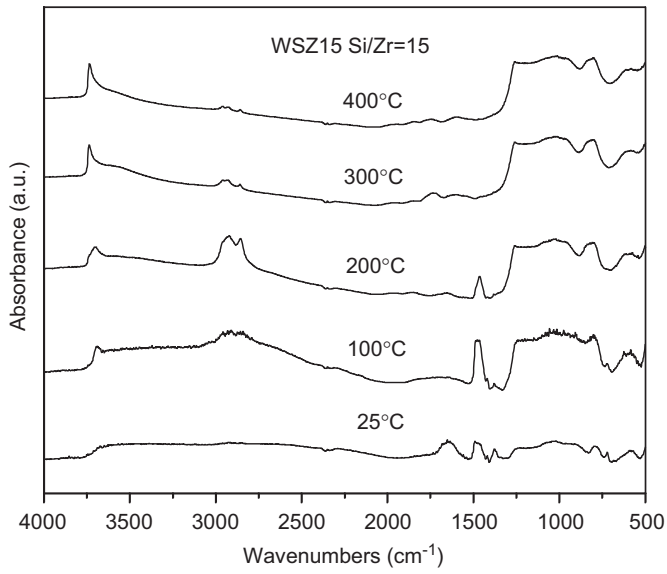

Fig. 2. A set of FTIR-*in situ* spectra of the sample Si/Zr = 15 at various temperatures.

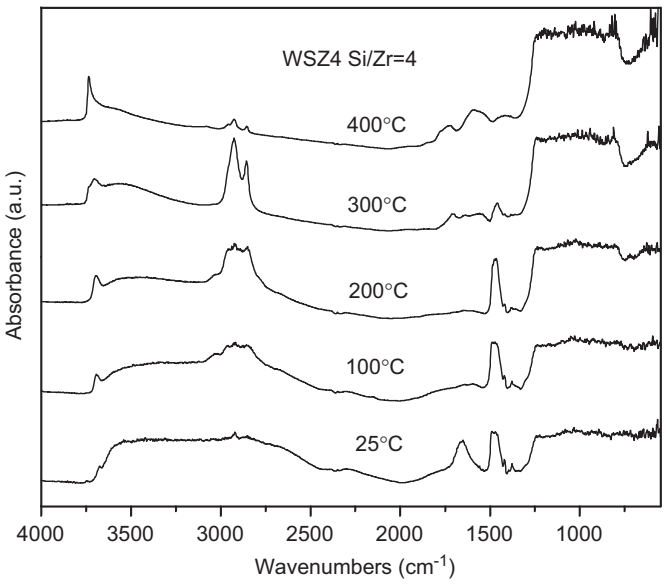

Fig. 4. A set of FTIR-*in situ* spectra of the sample Si/Zr = 4 at various temperatures.

calcined at various temperatures inside an IR cell, in order to analyze the changes of the surface properties and the surfactant incorporation into and removal from the solid. As an example, the IR spectra of the WSZ25 sample (Fig. 2) is discussed in detail. At 25 °C, a very broad absorption band covering the region between 3700 and 3000 cm^{-1} is observed, which is due to water adsorbed on the sample surface. The two small bands between 2950 and 2850 cm^{-1} are typical characteristics of the stretching vibrations of the C–H bond in the surfactant. There is an intense band located at 1650 cm^{-1}, which is assigned to the bending vibration of the OH bond. In the C–C stretching and C–H deformation vibration region, there are several bands located at approximately 1485, 1424 and 1377 cm^{-1}. These bands might be the result of bending mode vibrations (scissoring and rocking vibrations) of the C–H bonds in the $–CH_2–$ and $–CH_3$ groups in the surfactants [27,28]. In addition, the rocking vibration of the C–H bond in the $N–CH_3$ was observed at around 720 cm^{-1} [27,28]. The other bands below 1250 cm^{-1} are due to the fundamental vibrations of the Zr–O–Si (790 cm^{-1}) and Si–O–Si (1245, 810, 585 cm^{-1}) linkages in the framework [29]. These observations confirm that the surfactant cations were, indeed, incorporated into the solid network during the preparation and they were not completely removed in the washing step.

When the IR cell temperature was increased to 100 °C, the intensity of the wide band between 3700 and 3000 cm^{-1} remarkably decreased and a band at approximately 3690 cm^{-1} became visible. This band is assigned to the stretching frequency of the external silanol groups; while a group of bands at 2975, 2925 and 2850 cm^{-1} were observed. These bands correspond to C–H stretching bonds (νCH_{3as}, νCH_{2as} and $\nu(CH_{2as}+\nu CH_{3as})$) [30,31]. The intensity of these bands becomes sharper in comparison with the ones at 25 °C, however, when the covering effect produced by the broad band of the adsorbed water at 25 °C is taken into account, they remained almost unchanged. The bands at 1485, 1424 and 1350 cm^{-1}, related to vibrations of C–H bonds bending modes, also remained unchanged.

The intensity of the absorption band at 1650 cm^{-1} was strongly reduced at 100 °C, in a similar way to the change of the wide band between 3200 and 3600 cm^{-1}. These results indicate that most of the adsorbed water is desorbed; however, the incorporated surfactants have not been removed yet at 100 °C. A new band with low intensity appears at 3020 cm^{-1}, which is probably due to the stretching mode of the CH_3 group linked to the $-N(CH_3)_3^+$ polar heads of the surfactant [27,28].

When the temperature gained up to 200 °C and as the adsorbed water was further desorbed, the bands around 3700 cm^{-1}, and those at 2800–3000 and 1485 cm^{-1} clearly became sharper. At 300 °C, the bands at 1485, 1424 and 1380 cm^{-1} were remarkably reduced. At 400 °C, the group bands at 2800–3000 cm^{-1} were strongly reduced and the one at 1485 cm^{-1} disappeared. The band near 3700 cm^{-1} shifts its position towards the direction of higher energies, for example, it gradually shifted from 3690, 3712 and 3737 cm^{-1} when the temperature was increased from 100 to 200 and 300 °C, respectively; the intensity of these bands becomes sharper as the temperature increases. Some bands between 1800 and 1400 cm^{-1} appeared at a temperature above 300 °C. These bands might have originated from carbonate-like species resulting from the surfactant decomposition [31].

The FTIR spectra shown in Figs. 2–4 are very similar to Fig. 1. The assignments of the bands are the same as above. Compared to the other samples, the sample with Si/Zr = 4 has two relatively larger peaks at 1858 and 1735 cm^{-1} at 300 and 400 °C, indicating that more carbon-like materials are produced during the calcination. A high zirconium content in the solid might lead to a less-ordered structure, therefore, when the surfactant incorporated within the pores of such kind of material is removed, more coke-like materials might be produced. In addition, for the Si/Zr = 4 sample, the intensity of the band around 790–810 cm^{-1} is rather lower than those of the other three samples. Normally, this band is used to characterize the formation of the Si–O–Si bond. Several reasons may be responsible for it: first, the surface Si concentration in this sample is lower, thus the number of Si–O–Si bonds is less than in the other samples; second, the structure of this solid is rather disordered, as confirmed by XRD analysis and TEM observations shown in the following section, therefore, the intensity of the Si–O–Si bonds may be relatively lower; and third, the formation of more coke-like materials on this solid may cover some areas of the surface, thus the observed intensity of the Si–O–Si linkages is reduced.

3.1.2. XRD analysis

XRD patterns of mesoporous phases usually exhibit peaks in the low angle region. Fig. 5 shows the XRD patterns of the WSZ*n* samples calcined at 600 °C. The sample with Si/Zr = 25 (WSZ25) has two peaks that correspond to the (100) and (110) reflections of the solid, respectively. This XRD pattern is very similar to the Si-MCM-41 diffractogram, indicating that a small amount of zirconium ions incorporated into the Si-MCM-41 framework does not significantly modify the crystalline structure.

As the Si/Zr molar ratio decreased to 8 and 4, high order Bragg reflections were not well resolved. The (100) peak lost its sharpness and became rather broad. The intensity of the peak corresponding to the (110) planes is very low. It even disappeared, indicating that the regularity of the structure became rather poor. The channels in the ordered hexagonal arrangement were partially collapsed, in some degree, into disordered and wormhole-like packings. Therefore, too high zirconium content in the solid reduces the thermal stability and leads to a material with relatively low structural ordering. However, it is necessary to emphasize that, without any doubt, based on the nitrogen adsorption–desorption isotherm measurements, these materials are still mesoporous solids. Therefore, the broad diffraction peak may indicate a short-range ordering within the mesostructure.

3.1.3. Textural properties

The regular mesoporous structures of the WSZ*n* materials are manifested through their adsorption properties. Figs. 6–9

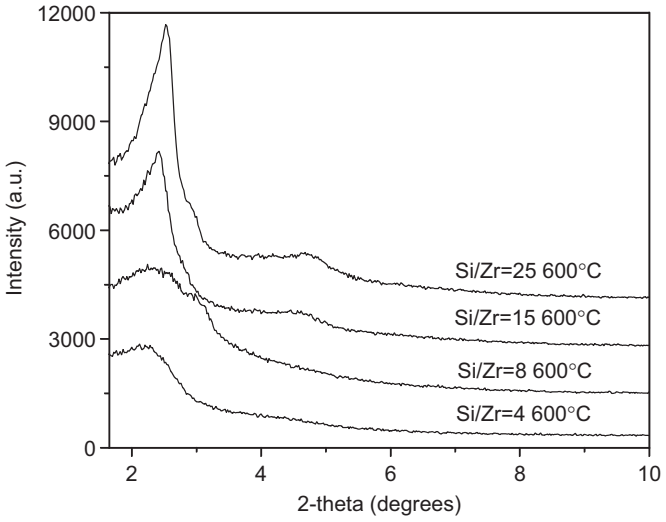

Fig. 5. XRD patterns of the Zr-MCM-41 solids prepared with different Si/Zr molar ratios. The samples were calcined at 600 °C.

show the N_2 adsorption–desorption isotherms of these samples as well as the pore diameter distributions. These are typical characteristics of mesoporous materials. The N_2 adsorption–desorption isotherms belong to type IV profiles.

There are three stages in the N_2 adsorption–desorption isotherms:

(1) The first stage ($p/p_0 < 0.2$) is due to a monolayer adsorption of nitrogen on the walls of the mesopores.
(2) The second stage ($0.2 < p/p_0 < 0.4$), characterized by a steep increase in adsorption, is due to a capillary condensation inside the mesopores. The p/p_0 at which the inflection starts is related to the diameter of the mesopores. The sharpness in this stage indicates a narrow pore size distribution.
(3) The third stage in the adsorption isotherm is the near horizontal section beyond the p/p_0 of 0.4, which is due to a multilayer adsorption on the outer surface of the particles.

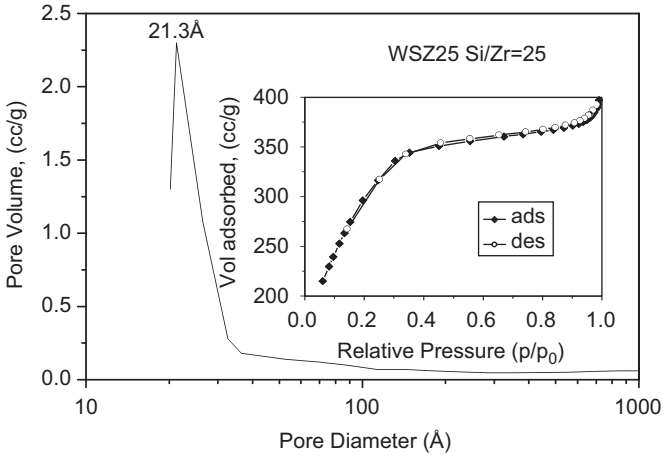

Fig. 6. Pore diameter distribution of the WSZ25 sample calcined at 600 °C. The inset is the N_2 adsorption–desorption isotherm of the sample.

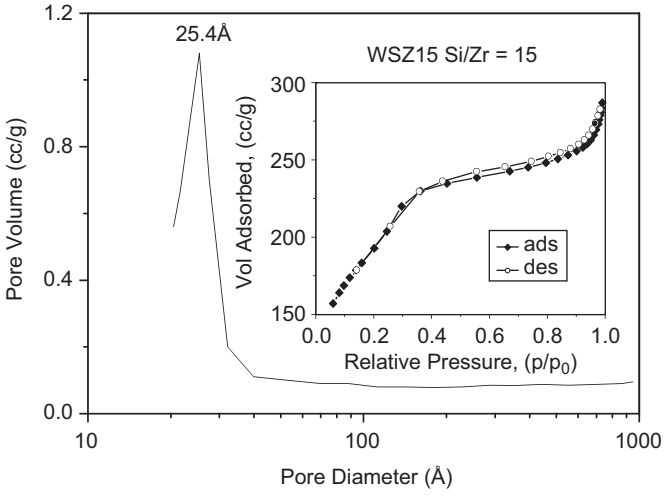

Fig. 7. Pore diameter distribution of the WSZ15 sample calcined at 600 °C. The inset is the N_2 adsorption–desorption isotherm of the sample.

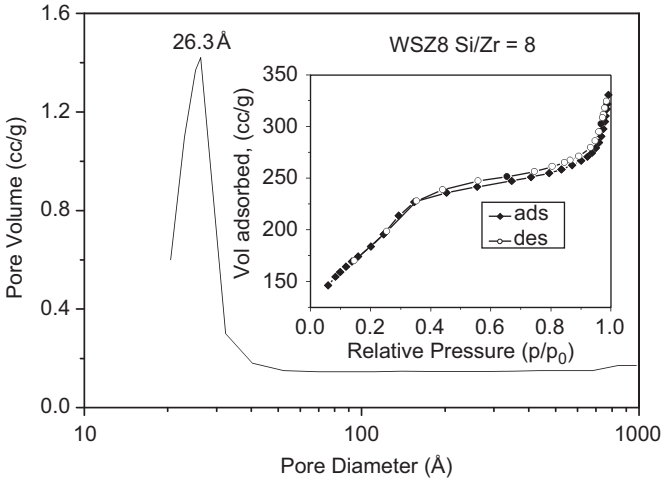

Fig. 8. Pore diameter distribution of the WSZ8 sample calcined at 600 °C. The inset is the N_2 adsorption–desorption isotherm of the sample.

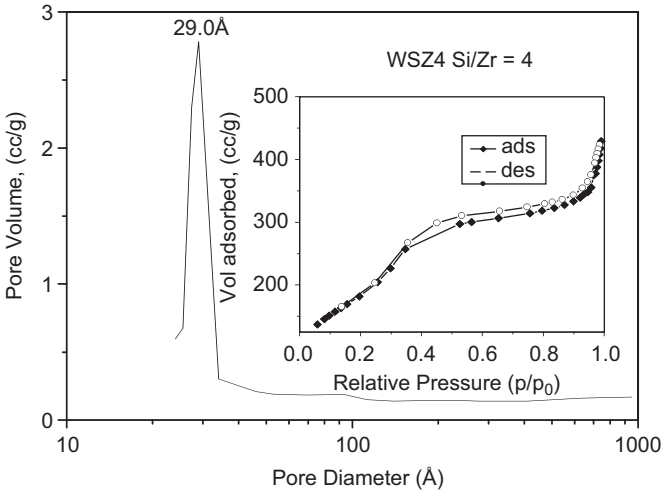

Fig. 9. Pore diameter distribution of the WSZ4 sample calcined at 600 °C. The inset is the N_2 adsorption–desorption isotherm of the sample.

The sharp step at p/p_0 relative pressures between 0.20–0.4 reveals the highly uniform mesoporous system. The shape and the sharpness of the isotherms vary with the zirconium content. For example, as the zirconium content in the materials increases, the sharpness of the second stage gradually decreases. In the WSZ25 solid, the lines of the N_2 adsorption and desorption isotherms are almost overlapped; however, they are gradually separated as the zirconium content increases. The coincidence of the adsorption and desorption lines can be ascribed to a similar mechanism for the two processes, which reflects the absence of pore blocking by the adsorbate. The absence of a hysteresis loop and the sharp curvature along the second stage, suggest the existence of uniform and cylindrical channels throughout the materials. The presence of large amount of any foreign species, such as possible extra-framework zirconium oxides in the channels of the solids would lead to an irreversible isotherm with a significant hysteresis loop.

Table 1
Textural properties of the WSZ*n* samples

Si/Zr molar ratio	Surface area (m^2/g)	Mean pore diameter (nm)	Pore volume (cm^3/g)
25	1113.9	2.16	0.4525
15	680.6	2.53	0.3263
8	654.8	2.93	0.4318
4	668.1	3.69	0.7209

The pore diameter distribution of the samples can also be seen in Figs. 6–9. The mean pore diameter varies with the Si/Zr molar ratio; it increases from 2.16 to 2.53, 2.93 and 3.69 when the Si/Zr molar ratio decreases from 25 to 15, 8, and 4, respectively. Therefore, increasing the zirconium content leads to increasing the pore diameter. However, the surface area decreases as the zirconium content increases until Si/Zr = 8. These observations show that zirconium incorporation strongly affects the textural properties of the resultant materials. The related textural data are reported in Table 1.

Usually, if foreign metals are deeply incorporated within the silica framework, some pore shrinkage or enlargement might occur, depending on the diameter of the foreign ions. The pore size can be increased by longer metal–oxygen bonds, such as in the case of Zr^{4+} ions inserted into the pore wall because the size of the Zr^{4+} ion ($r = 0.084$ nm) is much larger than that of the Si^{4+} ion ($r = 0.026$ nm). In the WSZ*n* samples, the pore size increased after zirconium incorporation. This result suggests that the Zr ions are indeed inserted into the silica framework.

3.1.4. Morphological features

The morphological features of the WSZ*n* materials calcined at 600 °C were studied by high-resolution TEM. Fig. 10(A) shows the TEM images of the WSZ15 solid. It is possible to see that the WSZ15 material contains ordered arrangements in most areas together with relatively disordered structures in some other regions. In the solid with high zirconium content, WSZ4, for example, rather disordered wormhole-like pores distributed along the whole region under observation were observed (Fig. 10(B)) and the pore diameter ranged between 2.6 and 3.0 nm. The Zr-modified MCM-41 mesoporous materials with high Si/Zr molar ratio are composed of many structural defects within an ordered hexagonal nano-channel matrix. On the other hand, the materials with low Si/Zr molar ratio or high zirconium content exhibit rather disordered mesostructures. These observations are in accordance to the XRD analysis indicating the formation of short-range ordered structures in the materials with high zirconium content.

3.1.5. ^{29}Si MAS-NMR spectroscopic analysis

Fig. 11 shows the ^{29}Si MAS-NMR spectra of the different WSZ*n* samples. A broad peak between −90 and −125 ppm was observed, which can be deconvoluted into three main components with chemical shifts at ca. −92, −103 and −115 ppm. These signals resulted from Q^2 (−92 ppm), Q^3 (−103 ppm) and Q^4 (−115 ppm) silicon nuclei, where Q^x corresponds to a silicon nuclei with x siloxane linkages, i.e., Q^2 to disilanol Si–(O–Si)$_2$(–O–X)$_2$, where X is H or Zr; Q^3 to silanol (X–O)–Si–(O–Si)$_3$ and Q^4 to Si–(O–Si)$_4$ in the framework [32,33]. The fractions of Q^2, Q^3 and Q^4 units and their relative values derived from

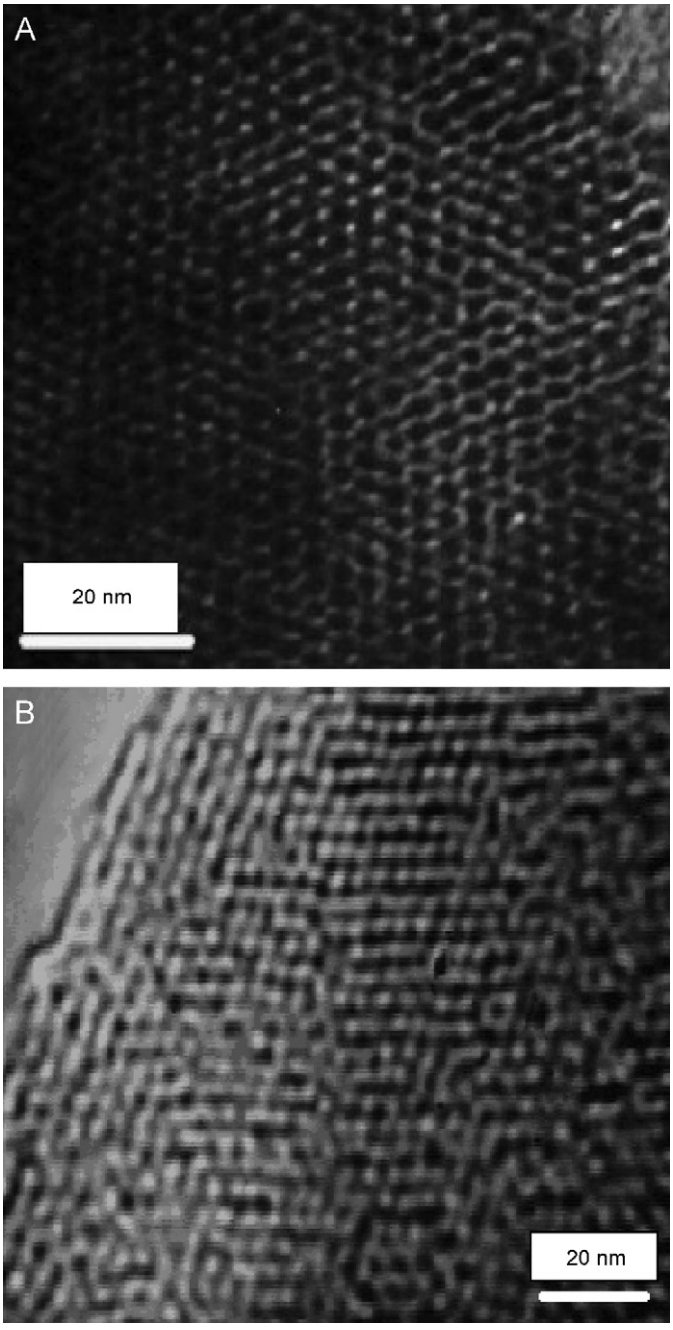

Fig. 10. TEM images of the WSZ*n* samples calcined at 600 °C. Relatively ordered hexagonal pores in most areas together with some disordered structures in some regions were observed in the WSZ15 sample (A); while, rather disordered wormhole-like pores distributed in the whole region studied were observed in the WSZ4 sample (B).

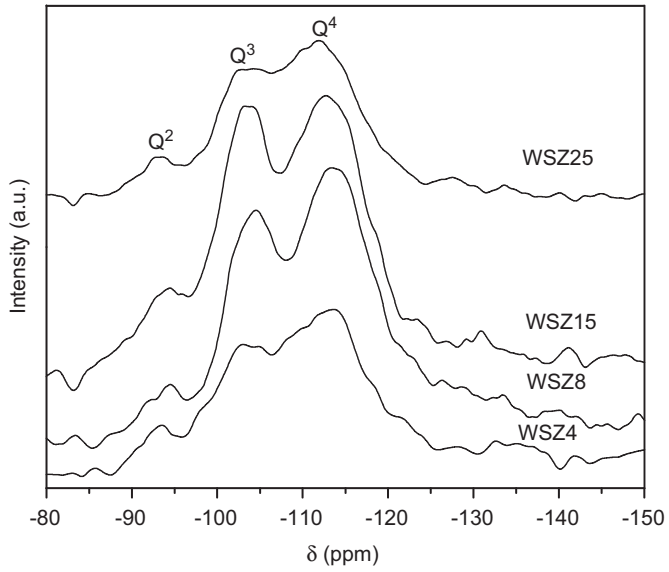

Fig. 11. A set of ^{29}Si MAS-NMR spectra of the WSZ*n* samples.

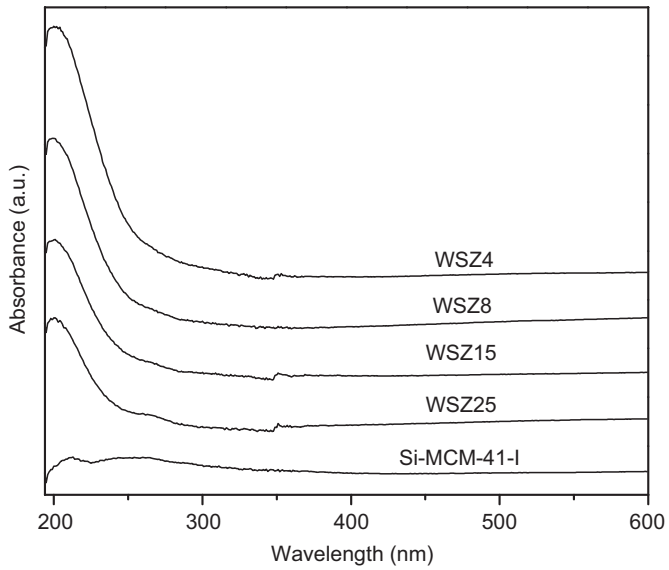

Fig. 12. The UV–vis spectra of the WSZ*n* samples and the Si-MCM-41-I sample as reference. The samples calcined at 600 °C were used for analysis.

Fig. 12 are shown in Table 2. The $(Q^3+Q^2)/Q^4$ values increase from 0.59 to 0.68 and 0.75 when the Si/Zr ratio vary from 25 to 15, 8 and 4, respectively. If compared to the 0.49 $(Q^3+Q^2)/Q^4$ value of the Si-MCM-41 solid, greater values of $(Q^3+Q^2)/Q^4$ in the WSZ*n* solids were obtained after the zirconium modification. These results also strongly indicate that some zirconium ions have been incorporated into the MCM-41 framework.

3.1.6. *Diffuse-reflectance UV–visible spectroscopic analysis*

The UV–visible spectroscopic technique is used to determine the local structure, e.g., the coordination state of the transition metal ions substituted in the matrix of the mesoporous molecular sieves. The UV–vis technique

Table 2
^{29}Si MAS-NMR data of WSZ*n* samples with various Si/Zr molar ratios

Si/Zr molar ratio	Q^4 (%)	Q^3 (%)	Q^2 (%)	$(Q^3+Q^2)/Q^4$
∞*	67.0	29.4	3.6	0.49
25	62.8	32.1	5.1	0.59
15	59.7	34.5	5.8	0.68
8	59.7	35.1	5.2	0.68
4	57.1	36.3	6.6	0.75

∞*: Si-MCM-41.

measures the scattered light reflected from the surface of the samples in the UV–visible range (200–800 nm). For most of the isomorphously substituted mesoporous molecular sieves, transitions in the UV region (200–400 nm) are of particular interest. Fig. 12 presents the UV–vis spectra of the WSZ*n* samples calcined 600 °C along with the Si-MCM-41 sample as reference. In general, the absorption edge of zirconium oxide-based powders is due to the $O^{2-} \rightarrow Zr^{4+}$ charge-transfer transition, corresponding to the excitation of electrons from the oxygen valence band (2*p* character in the O ion) to the zirconium conduction band (4*d* character in the Zr ion). The zirconium in various types of oxides presents different coordinations being 6-, 7- or 8-fold, with examples provided by perovskite-type $SrZrO_3$ (6-fold), baddeleyite-type zirconia (7-fold) and cubic zirconia and $ZrSiO_4$ (8-fold). The position of the absorption edge is located at a low energy region for octahedral Zr^{4+} (inflection point near 300 nm for perovskite), at a middle energy region for the hepta-coordinated Zr^{4+} of monoclinic ZrO_2 (inflection point near 240 nm) and at a high energy region for the eight-coordination Zr^{4+} (inflection point near 220 nm) [34,35].

In our case, all the Zr-containing samples exhibit a broad band with a maximum near 199 nm attributable to a charge-transfer transition from oxygen to an isolated Zr(IV) cation in a tetrahedral environment (Fig. 12). The peak intensity significantly increased with the increase of the zirconium content. The Si-MCM-41 sample did not show any significant absorption peak in the same region. As discussed above, in neat monoclinic ZrO_2 where, obviously, no isolated Zr atoms exist, the charge transition from oxygen to metal usually takes place at approximately 240 nm. These results suggest that the zirconium ions in our samples are in a different state from that in the pure ZrO_2 solid, which strongly indicates that no segregated zirconia phase is formed in our samples and all the zirconium ions, therefore, are incorporated into the framework of the silica mesoporous materials. This conclusion is also supported by XRD analysis in the wider 2θ range between 10° and 80° where no diffraction peak corresponding to a pure crystalline ZrO_2 phase was observed (not shown).

A slight shift in the position of the band towards higher energies in comparison with the one shown in the Si-MCM-41 sample is attributed to the monatomic distribution of zirconium ions in the Zr-containing solids. A similar

shift in the charge-transfer band was previously reported in Ti-containing MCM-41 samples [36].

3.1.7. Surface acidity of the WSZn samples

The *in situ* FTIR spectra of pyridine adsorption of the WSZ*n* samples with various Si/Zr molar ratios are shown in Figs. 13–16. The absorption bands corresponding to pyridine adsorbed on Lewis acid sites were observed at 1450 and 1590 cm^{-1} for the sample with a molar ratio of Si/Zr = 25. In addition, a band at 1490 cm^{-1} was also formed, which corresponds to pyridine associated with both, Lewis and Brönsted acid sites. A weak band at 1540 cm^{-1} appeared, indicating the formation of a small number of Brönsted acid sites in this sample [37]. The one at 1640 cm^{-1} was assigned to pyridine adsorbed on the hydroxyls ions. When the sample was degassed at 100 °C, these bands remained unchanged. However, at 200 °C, all the bands almost disappeared, indicating that the interaction between pyridine and the sample is weak, and thus the acid strength is rather weak.

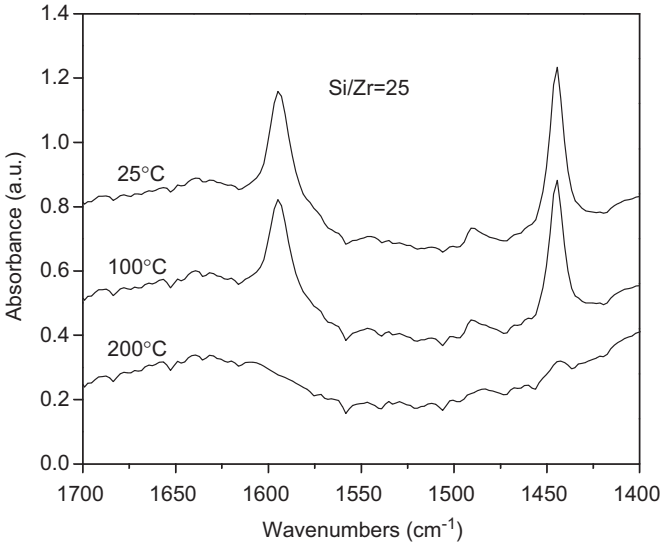

Fig. 13. FTIR-*in situ* spectra of pyridine adsorption on the WSZ25 sample.

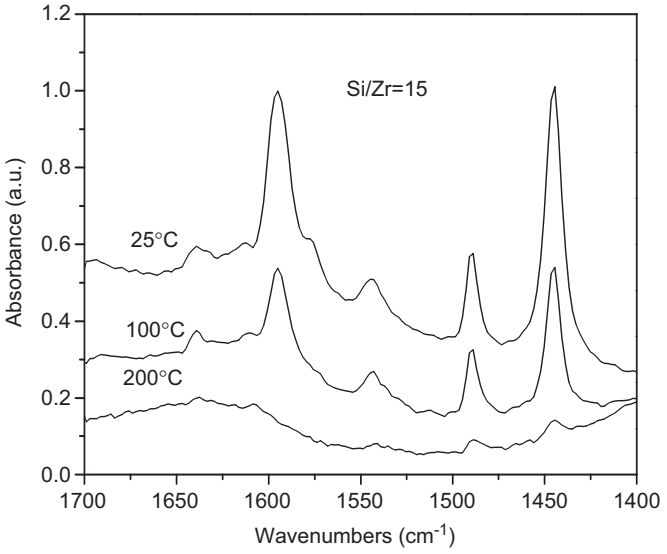

Fig. 14. FTIR-*in situ* spectra of pyridine adsorption on the WSZ15 sample.

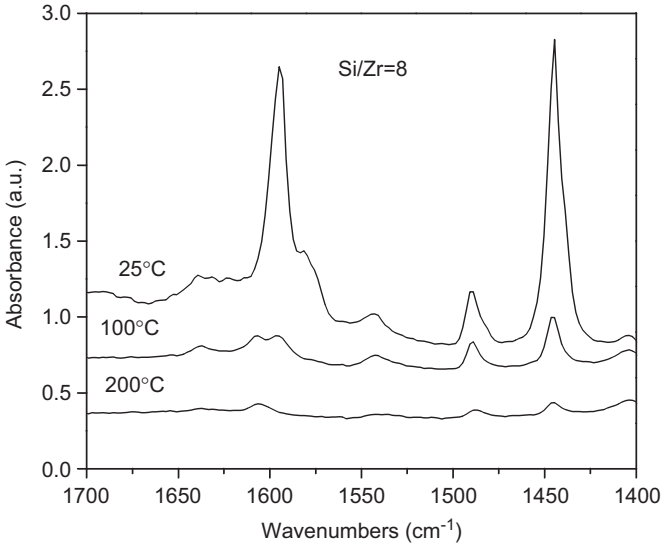

Fig. 15. FTIR-*in situ* spectra of pyridine adsorption on the WSZ8 sample.

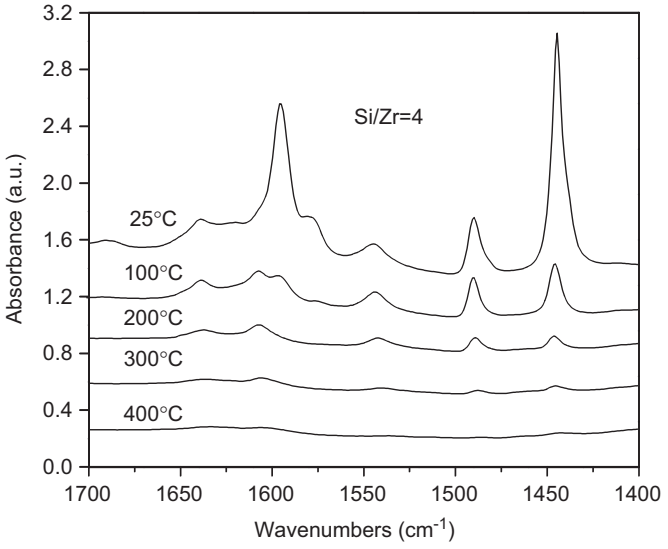

Fig. 16. FTIR-*in situ* spectra of pyridine adsorption on the WSZ4 sample.

Similar to the Si/Zr = 25 sample, Lewis acid sites were also formed on the sample with a Si/Zr molar ratio of 15, characterized by the absorption bands at 1445, 1580 and 1598 cm^{-1}. The band corresponding to pyridine associated with both, Lewis and Brönsted acid sites was also observed at 1490 cm^{-1}. Brönsted acid sites appeared in this sample as indicated by the band at 1540 cm^{-1}. As the heating temperature was raised to 100 °C under vacuum, the intensities of all the bands lowered. At 200 °C, they almost disappeared.

As the Si/Zr molar ratio decreased to 8, the intensities of the bands corresponding to the Lewis acid sites and

Brönsted acid sites were remarkably increased compared to those of the samples with Si/Zr molar ratios of 25 and 15, indicating that a larger population of acid sites were formed on the sample with high zirconium content. The acid strength was also enhanced because all the bands were stable up to 250 °C under vacuum condition. After degassed at 400 °C, all the bands entirely disappeared, indicating that the adsorbed pyridine was completely removed from the sample. The behavior of pyridine adsorption on the sample WSZ4 is similar to that of sample WSZ8. Therefore, the number of Lewis and Brönsted acid sites and the acid strength are similar for these two samples.

As mentioned above, the Zr^{4+} ion diameter is much larger than that of the Si^{4+} ion. When the smaller Si^{4+} ions are replaced by the larger Zr^{4+} ions in the framework of the solid, the Zr–O–Si bond length clearly differs from that of Si–O–Si, and this must lead to structural distortion or deformation. Because many silanol groups exist in the structure of the solids, the presence of small amounts of zirconia may affect the strength of the SiO–H bonds. Changes in the electron density around Si, due to charge unbalance, to differences in electronegativity or to local structural deformation produced by the introduction of Zr^{4+} ions into the vicinity of the hydroxyl-carrying silicon, may weaken the SiO–H bond [38]; this is one of the possible origins giving rise to the Brönsted acid sites on the Zr-modified mesoporous materials.

Table 3 shows the acidity data of the various WSZ*n* samples. Obviously, as the zirconium content increases, the Brönsted acidity linearly increases. It is worthwhile to note that if compared to the pure Si-MCM-41 sample, the incorporation of a proper amount of zirconium may significantly enhance the surface acidity and creates Brönsted-type acid sites in the solid.

It is noteworthy that It is possible that at 25 °C, the adsorption might include some physical adsorption of pyridine molecules. However, the IR spectra were recorded after the samples were outgassed; therefore, most pyridine molecules that may have been physically adsorbed should be removed. On the other hand, it is seen in the FTIR spectra that the bands corresponding to Brönsted acid sites remained almost unchanged when the temperature rose from 25 to 100 °C. In the present work, special attention was paid on the Brönsted acidity, therefore, it seems that there is no significant difference when we take into account the data obtained at 25 or 100 °C.

Table 3
Acidity of the WSZ*n* samples in relation with the Si/Zr molar ratio

Si/Zr molar ratio	Brönsted acid sites (μmol/g)	Lewis acid sites (μmol/g)	Total acid sites (μmol/g)
∞*	0	658	658
25	11	1008	1019
15	82	1035	1117
8	70	1217	1287
4	142	1134	1276

∞*: Si-MCM-41.

3.2. The Pt/HPW/WSZn catalysts

Although the incorporation of zirconium ions into the Si-MCM-41 solids improves the surface acidity, it seems not enough for acid catalytic reactions like the isomerization of hydrocarbons, where strong proton-type acidity is required. In order to further increase the surface acidity, 25 wt% of the $H_3PW_{12}O_{40}$ heteropolyacid was dispersed on the Zr-MCM-41 solids. In the following sections, results of the surface acidity, variations of the *Keggin* structure and the morphological features of the 1 wt%Pt/25 wt%$H_3PW_{12}O_{40}$/WSZ*n* catalysts are reported.

3.2.1. Skeletal FTIR studies

The FTIR spectra of the various catalysts were investigated in order to collect information on the structural features of the supported $H_3PW_{12}O_{40}$ for assessing the nature of the interaction between the HPW and the support. Because the IR spectra of both, the support and the Pt/$H_3PW_{12}O_{40}$/WSZ25 catalyst are very similar, in order to clearly show the net contribution from the dispersed $H_3PW_{12}O_{40}$, the IR spectrum of the Pt/$H_3PW_{12}O_{40}$/WSZ25 catalyst was subtracted from that of the WSZ25 support, as shown in Fig. 17. The four fingerprint absorption bands of the heteropolyanion vibrations at approximately 1080, 982, 893 and 822 cm^{-1} present in the pure $H_3PW_{12}O_{40,}$ were mostly retained [39,40]. The P–O symmetric stretching is indicated by the vibration transition at 1080 cm^{-1}. The normal mode associated with the band at 982 cm^{-1} is defined predominately by the W=O_d stretch mode. The bands at 893 and 822 cm^{-1} are associated with the stretching motion of

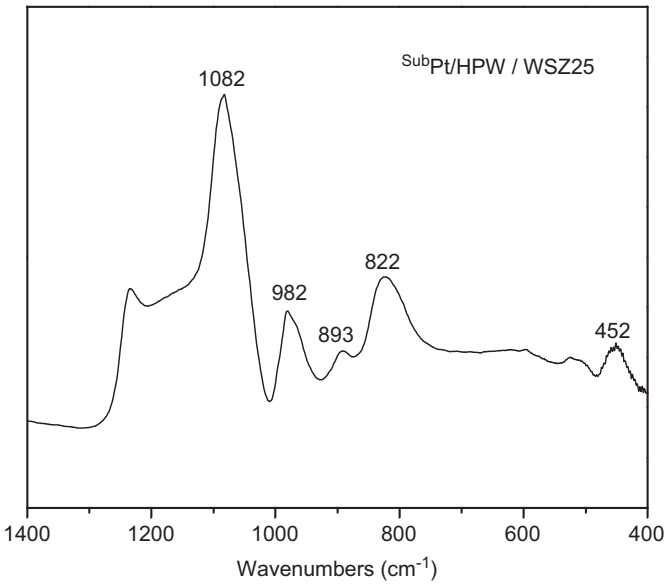

Fig. 17. Subtraction of the Pt/$H_3PW_{12}O_{40}$/WSZ25 FTIR spectrum from that of the WSZ25.

W–O–W bridges. The band at 893 cm^{-1} is described as a W–Oc–W stretch mode (inter-bridges between corner-sharing octahedral) and the band at 822 cm^{-1} is attributed to W–O_e–W stretch mode (intra-bridges between edge-sharing octahedral).

However, the fingerprint bands in the Pt/$H_3PW_{12}O_{40}$/WSZ25 catalyst experienced a shift towards higher frequencies and broadening, relative to those of the pure heteropolyacid (not shown), indicating the high dispersion of the heteropolyacid on the support. Similar FTIR spectroscopic features were also observed in the other three Pt/$H_3PW_{12}O_{40}$/WSZ*n* samples. Therefore, it can be concluded that the heteropolyacid $H_3PW_{12}O_{40}$ retains its basic structure without strong modifications after dispersed on the Zr-MCM-41 solids.

3.2.2. *UV–visible spectroscopic analysis*

The UV–vis spectra of the pure HPW and the Pt/HPW/WSZ*n* catalysts are shown in Fig. 18. The pure HPW has three peaks around 252, 300 and 350 nm. The bands near 250 and 300 nm are due to the $O^{2-} \rightarrow W^{6+}$ charge transfer of the polyoxotungstate at W–O and W=O bonds, respectively. As for the one at 350 nm, it is mostly related to crystalline water [41]. It is noted that, for the HPW supported catalysts, two peaks were also observed at approximately 199 and 260 nm. Relative to the pure HPW, the absorption bands of the Pt/$H_3PW_{12}O_{40}$/WSZ*n* catalysts significantly shift their positions to a lower wavelength range, which indicates the very high dispersion of the heteropolyacid on the Zr-MCM-41 support. Generally, for nanoparticles in the quantum dot range, the frequency of the absorbed light usually shifts towards a lower wavelength as the particle diameter decreases. This can be proved by considering Eq. (1). The energy change of a spherical quantum dot can be expressed as

$$\Delta E = h^2/8R^2(1/m_e + 1/m_h), \quad (1)$$

where ΔE is the energy change in the band gap due to the quantum size effect, h is the Planck constant, R is the radius of the quantum dot, m_e is the effective mass of an electron and m_h is the effective mass of a hole. It is clear that the absorption energy of the quantum dot will shift to a higher frequency (or to a lower wavelength) as the value of R decreases.

It is noteworthy that since the UV–vis analysis was carried out at ambient temperature and the pure $H_3PW_{12}O_{40}$ sample used was not thermally pretreated before the experiment, thus crystalline water molecules linked to the heteropolyacid crystals are contained in the structure, a different situation from the Pt/$H_3PW_{12}O_{40}$/WSZ*n* catalysts which were calcined at 300 °C. The peak position shift is probably also affected by the removal of water molecules from the crystalline structure.

3.2.3. *^{31}P MAS-NMR spectroscopic analysis*

The ^{31}P MAS-NMR spectra of the Pt/HWP/Zr-MCM-41 samples with various Si/Zr molar ratios are shown in Fig. 19. The pure $H_3PW_{12}O_{40}$ sample presents one single narrow signal at approximately −15 ppm (not shown). However, for the $H_3PW_{12}O_{40}$ supported on Zr-MCM-41 samples, several peaks at approximately −12.5, −13.7 and −15.2 ppm were observed.

It has been reported that $H_3PW_{12}O_{40}$ supported on TiO_2, has four peaks at around −4, −8, −11 and −13 ppm, corresponding to adsorbed phosphorus species derived from a highly fragmented *Keggin* unit, a partially fragmented unit and a deformed *Keggin* structure interacting with surface hydroxyl groups, respectively [42]. The unsupported $H_3PW_{12}O_{40}$ shows a single and sharp peak around −15 ppm. On the basis of NMR results of pure heteropolyacids and $H_3PW_{12}O_{40}$ on TiO_2, we postulate the

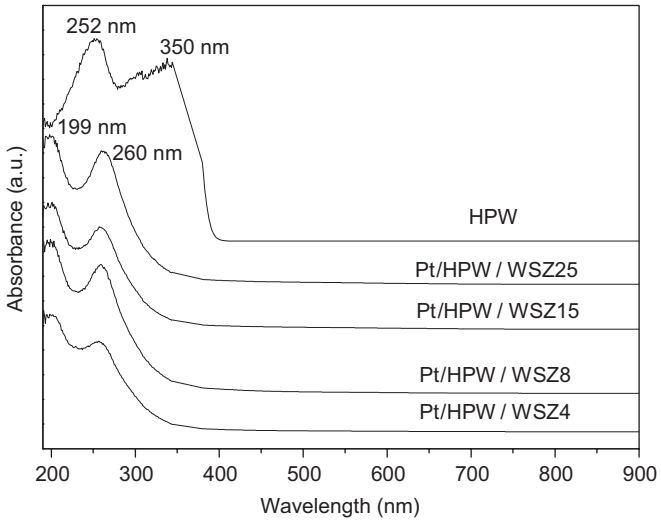

Fig. 18. UV–vis spectra of the pure HPW and the Pt/HPW/WSZ*n* catalysts.

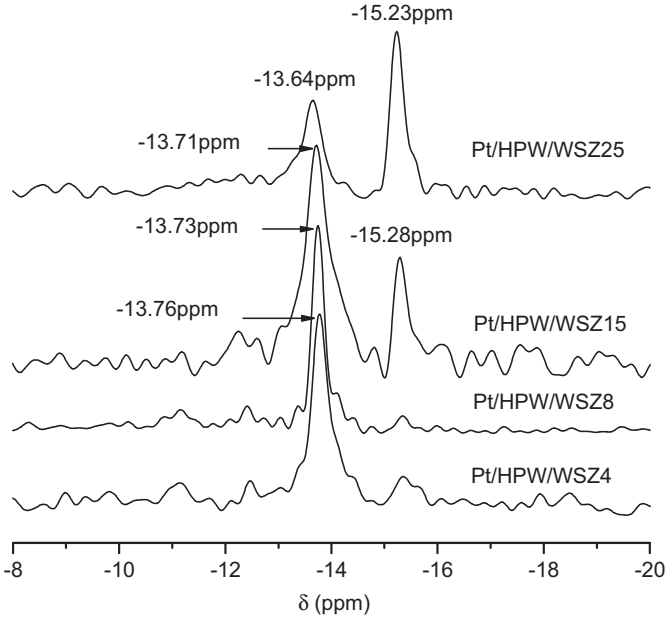

Fig. 19. ^{31}P MAS-NMR spectra of the Pt/HPW/WSZ*n* catalysts.

formation of different structures of the dispersed heteropolyacids formed on the $Pt/H_3PW_{12}O_{40}/WSZn$ catalysts according to three different NMR signals:

(i) The peak at −15.2 ppm is due to a bulk-like structure of $H_3PW_{12}O_{40}$ crystals, which indicates that, on the surface of the Zr-MCM-41 solids, there are some bulk-like clusters or $H_3PW_{12}O_{40}$ particles.
(ii) The peak at −13.7 ppm might indicate that part of the *Keggin* structure was deformed or distorted due to strong interactions with the support, but the fundamental *Keggin* structure was preserved.
(iii) The small band at −12.5 ppm might be attributed to defect *Keggin* species caused by the partial fragmentation of the heteropolyacid structure due to the strong interaction with surface hydroxyl groups in the support. However, this band is very weak in intensity, it is a little more apparent for the sample Pt/HPW/WSZ15; if one looks at the right side of the spectra, there are other peaks at the same level of intensity, thus, the peak at −12.5 ppm is probably noisy.

It can be seen in Fig. 19 that the intensity of the peak at −15.2 ppm decreases as the zirconium content increases. On the other hand, the intensity of the band at −13.7 ppm shown in the samples with higher zirconium content increases in comparison with that of Pt/HPW/WSZ25. These changes reflect the variation of the amount of these two different kinds of *Keggin* species on the support. The higher the zirconium content in the solid, the stronger the interaction between the heteropolyacid and the support, and thus more heteropolyacid species with distorted or deformed *Keggin* structure can be formed on the support.

The formation of the deformed or distorted *Keggin* species might be related to the nature of the surface of the support, for example, the existence of hydroxyls, similar to the observation of heteropolyacid supported on the SiO_2 [43]. Heteropolyacid molecules may react with hydroxyl ions by protonation or proton-transfer, as expressed by the following Eqs. (2) and (3):

Protonation of surface *M*–OH groups followed by dehydration was suggested ($1<m<3$):

$$H_3PW_{12}O_{40} + m(\equiv M-OH) \rightarrow (\equiv M)_m^+(H_{3-m}PW_{12}O_{40})_m^- + mH_2O, \quad (2)$$

where M = Si or Zr.

The interaction species may be also formed by proton-transfer, according to reaction (3):

$$H_3PW_{12}O_{40} + \equiv M-OH \rightarrow (\equiv M-OH_2)^+ + (H_2PW_{12}O_{40})^-. \quad (3)$$

3.2.4. Morphological features

High-resolution TEM analysis was performed on the Pt/HPW/WSZ*n* samples in order to observe the location and size of the heteropolyacid species as well as to study the pore system of the catalysts. Fig. 20 shows the TEM images corresponding to the Pt/HPW/WSZ solids. On the surface of the Pt/HPW/WSZ8 catalyst, the distribution of the nanoparticles is very homogeneous along most regions of the sample, most of the regions are covered with dark-colored fine particles (Fig. 20(A)), indicating the high dispersion of the supported heteropolyacid. The crystalline structure of the support remains almost unchanged. A close observation clearly reveals pores of 2–3 nm in diameter in the Pt/HPW/WSZ4 catalyst, but their openings are partially covered with web-like materials (Fig. 20(B) and (C)). EDS analysis confirms that these dispersed materials belong to the heteropolyacids together with metallic Pt particles (Fig. 21). The separated Pt particles cannot be observed, indicating that the metallic Pt particles are mixed with heteropolyacids. Some of the pores are partially blocked by these Pt–heteropolyacid deposits. The boundary of some regions or particles is rather rough because of the embedment of many islands of approximately 2 nm diameter. Apparently, most of the heteropolyacid particles are located on the pore openings. These TEM images show that the dispersion of the heteropolyacids is rather homogeneous and large aggregates of heteropolyacids are not observed.

3.2.5. Surface acidity of the Pt/HPW/WSZn catalysts

Figs. 22–25 show a set of *in situ* FTIR spectra of the pyridine adsorption on the 1 wt% Pt/25 wt% $H_3PW_{12}O_{40}$/WSZ*n* ($n = 25$, 15, 8, 4) catalysts. Lewis acid sites were formed on the surface of all the samples as characterized by the bands at 1445, 1578 and 1595 cm^{-1}. Brönsted acid sites were also formed as indicated by the absorption bands at 1545 and 1637 cm^{-1}. In addition to these bands, a band corresponding to pyridine associated with both, Lewis and Brönsted acid sites, was observed at 1490 cm^{-1} (noted as B + L acid sites).

When the catalysts were heated inside the IR cell under vacuum from 50 to 100 and to 200 °C, the intensities of all the bands corresponding to Brönsted acid sites slightly lowered. They were further reduced after calcination at 300 °C and their disappearance took place above 400 °C.

The acidity data calculated from the FTIR spectra in Figs. 22–25 are reported in Table 4. In comparison with the pure Zr-MCM-41 support, the total acidity of the samples was slightly increased or slightly reduced, depending on the Si/Zr molar ratio. However, the number of Brönsted acid sites was greatly increased after heteropolyacid impregnation, for example, for the catalyst with the Si/Zr = 25 support, the Brönsted acid sites are 141 μmol/g, which is 14 times greater than those of the WSZ25 support, where only 11 μmol/g Brönsted acid sites were formed. It is also noteworthy that the acid strength is remarkably improved after $H_3PW_{12}O_{40}$ impregnation. The Zr-MCM-41 support samples usually loose their acidity after thermal treatment

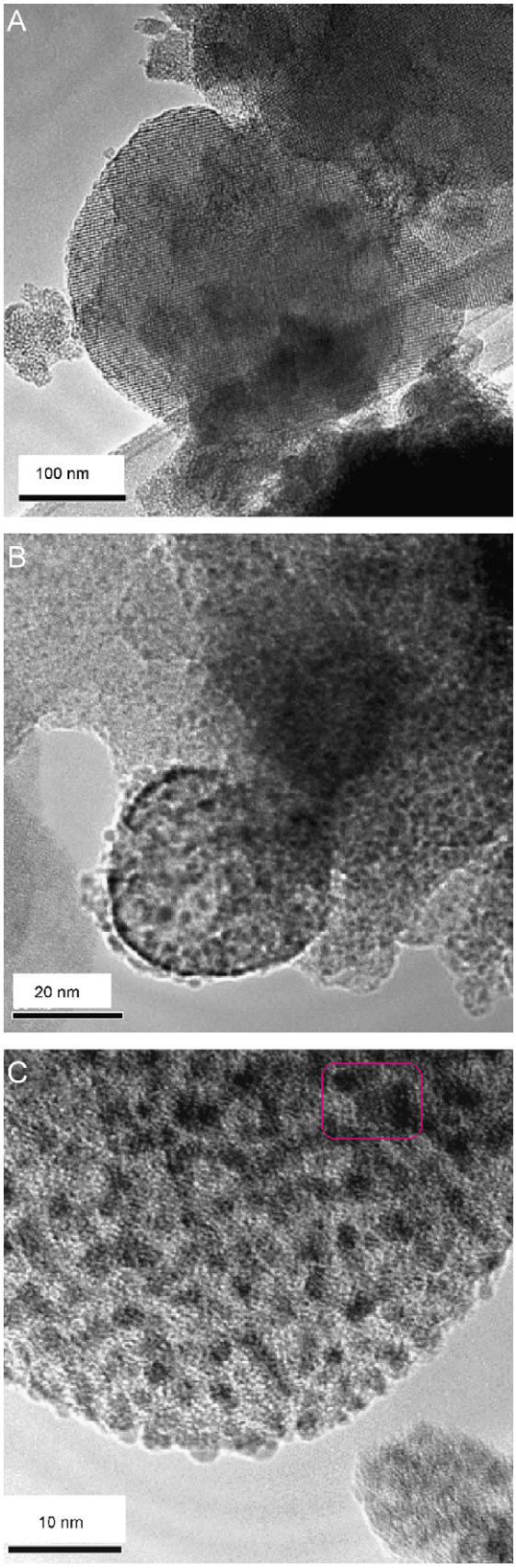

Fig. 20. High-resolution TEM images of (A) and (B) (Pt/HPW/WSZ4) and (C) (Pt/HPW/WSZ8) materials.

at 200 °C, however, in the heteropolyacid-doped catalysts, the acidity can be retained at 400 °C.

The composition of the support has a strong effect on the acidity of the catalysts. As the Si/Zr ratio in the support decreased from 25 to 15, 8, and 4, the Brönsted acidity proportionally increased from 141 to 201, 223 and 236 μmol/g, respectively (Table 4). This means that increasing the zirconium content in the support linearly increases the Brönsted acidity. Considering the slight reduction of the total acidity after heteropolyacid impregnation, we may conclude that heteropolyacid impregnation mainly enhances the Brönsted acid sites while slightly inhibits the Lewis acid sites (by deposition on them), particularly in the catalysts with high zirconium content. The zirconium content also strongly affects the acid strength; high zirconium content significantly improves the strength of both, Lewis and Brönsted acid sites.

These novel heteropolyacid supported catalysts with mesopores and strong Brönsted acidity have been proved to be excellent for the hydroisomerization of *n*-heptane, the molar ratio of the multibranched to monobranched isoheptanes in the products reaches as high as 0.8–1.2, which is 2–4 times higher than that obtained from the catalysts using microzeolites as support, tested under similar reaction conditions. The related catalytic results will be reported in a separate paper [44].

4. Conclusions

Zr-based MCM-41 mesoporous molecular sieves with hexagonal channels have been synthesized by using low-cost fumed silica as Si source through a surfactant-templated approach. The removal of the cationic surfactants incorporated into the Zr-MCM-41 framework during the synthesis can be clearly monitored by the *in situ* FTIR technique. The structural regularity of the solids is strongly affected by the Si/Zr molar ratio and the calcination temperature. The ordered mesoporous structures of as-made Zr-MCM-41 samples can transform into relatively disordered wormhole like pore systems after calcination at 600 °C. A high zirconium content, i.e. Si/Zr = 4, is unfavorable to the formation of Zr-MCM-41 with highly ordered mesostructure.

Brönsted acid sites were created in the solids after zirconium incorporation into the Si-MCM-41 framework. Both, the acid strength and the number of Brönsted acid sites significantly increased as the zirconium content increased. When the heteropolyacid $H_3PW_{12}O_{40}$ was impregnated onto the Zr-MCM-41 supports, the Brönsted acidity of the Pt/HPW/WSZn catalysts was remarkably enhanced by 2–10 times relative to that of the bare Zr-MCM-41 supports. Two kinds of heteropolyacids were formed on the surface of the catalysts: (i) bulk-like heteropolyacid particles with unchanged *Keggin* units; (ii) highly dispersed heteropolyacids with a distorted *Keggin* structure.

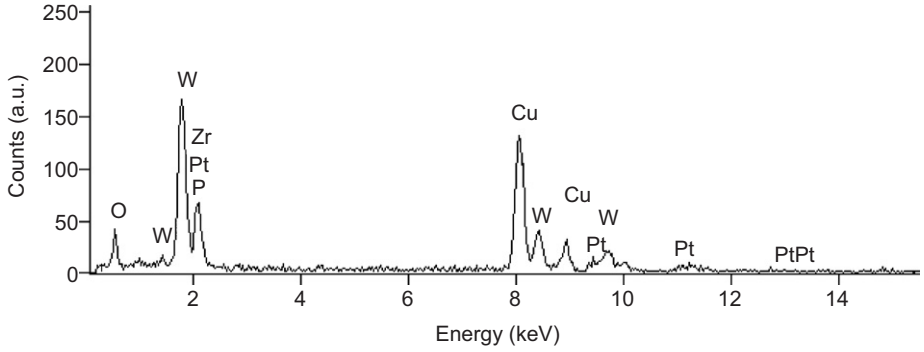

Fig. 21. An EDS spectrum corresponding to the marked area in TEM image (C), showing coexistence of metallic Pt and Keggin unit of the heteropolyacid in the investigated area.

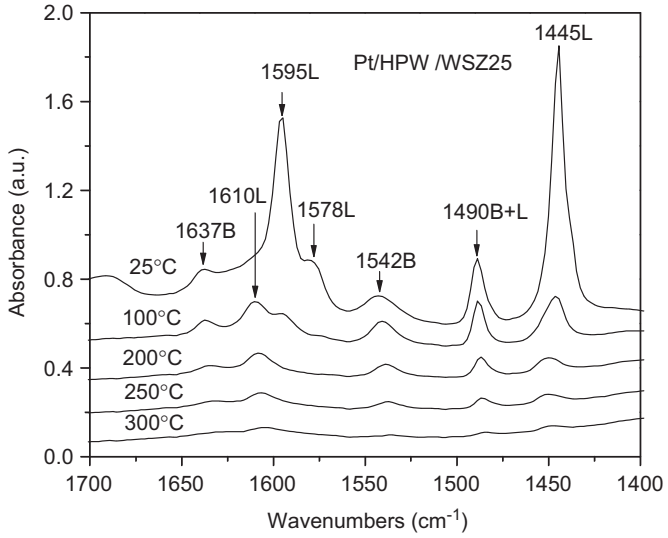

Fig. 22. FTIR-*in situ* spectra of pyridine adsorption on the Pt/HPW/WSZ25 catalyst.

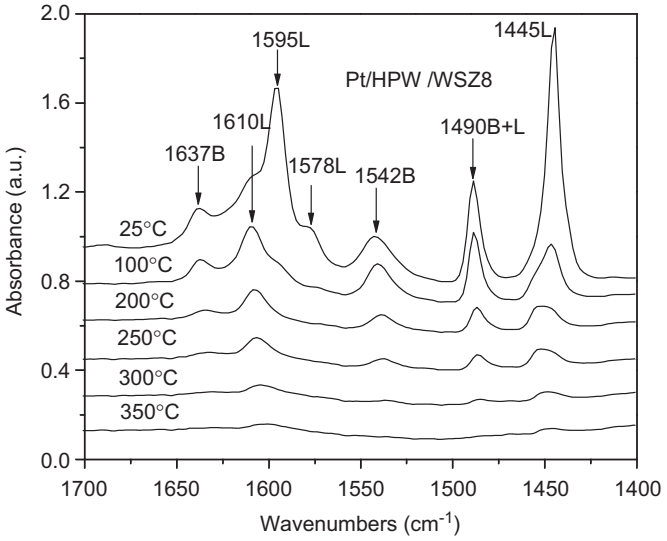

Fig. 24. FTIR-*in situ* spectra of pyridine adsorption on the Pt/HPW/WSZ8 catalyst.

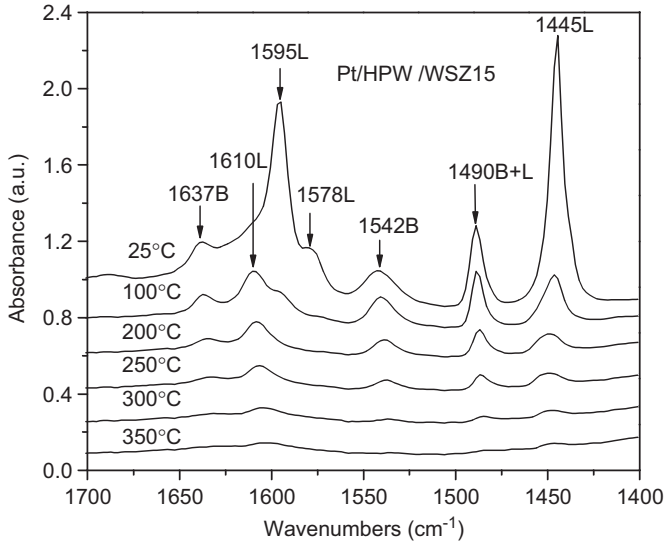

Fig. 23. FTIR-*in situ* spectra of pyridine adsorption on the Pt/HPW/WSZ15 catalyst.

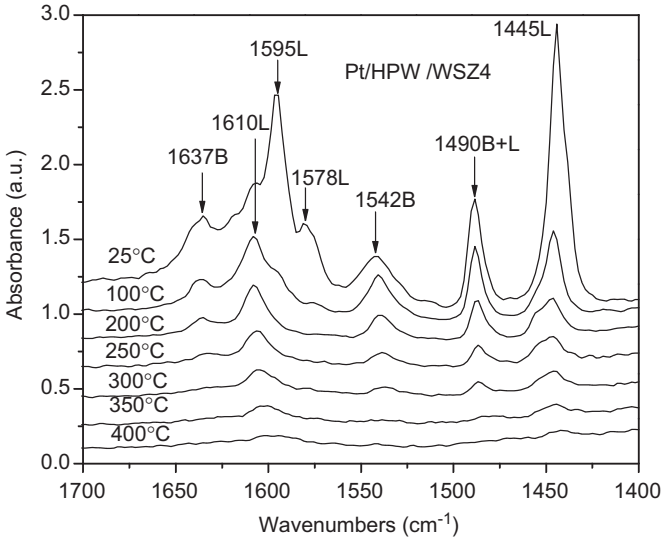

Fig. 25. FTIR-*in situ* spectra of pyridine adsorption on the Pt/HPW/WSZ4 catalyst.

Table 4
Acid properties of the Pt/HPW/WSZ*n* ($n = 25, 15, 8, 4$) catalysts

Si/Zr molar ratio	Brönsted acid sites (μmol/g)	Lewis acid sites (μmol/g)	Total acid sites (μmol/g)
25	141	1159	1300
15	201	1065	1266
8	223	889	1112
4	236	943	1179

Acknowledgments

L.F. Chen wishes to acknowledge the scholarship for her study of the doctorate degree offered by the CONACyT-Mexico. The financial support from the projects CGPI-IPN-2006067 and CONACyT (Mexico)-NSF (China) J110.426/2005 is appreciated. The authors would like to thank Dr. P. Pérez and Dr. I. Hernández for their help in the characterization of the samples.

References

[1] A. Galarneau, D. Desplantier-Giscard, F. Di Renzo, F. Fajula, Catal. Today 68 (2001) 191.
[2] V. Yu. Gusev, X. Feng, Z. Bu, G.L. Haller, J.A. O'Brien, J. Phys. Chem. 100 (1996) 1985.
[3] A. Corma, V. Fornes, M.T. Navarro, J. Perez-Pariente, J. Catal. 148 (1994) 569.
[4] T. Okuhara, N. Mizuno, M. Misono, Appl. Catal. A: Gen. 222 (2001) 63.
[5] S. Biz, M.L. Occelli, Catal. Rev.-Sci. Eng. 40 (1998) 329.
[6] F. Marme, G. Couduruer, J.C. Védrine, Microporous Mesoporous Mater. 22 (1998) 151.
[7] J.A. Dias, E. Caliman, S.C.L. Dias, M. Paulo, A.T.C.P. de Souza, Catal. Today 85 (2003) 39.
[8] R. Mokaya, W. Jones, Z. Luan, M.D. Alba, J. Klinowski, Catal. Lett. 37 (1996) 113.
[9] R. Schmidt, D. Akporiaye, M. Stöcker, O.H. Ellestad, J. Chem. Soc. Chem. Commun. (1994) 1493.
[10] W. Zhang, M. Fröba, J. Wang, P.T. Tanev, J. Wong, T.J. Pinnavaia, J. Am. Chem. Soc. 118 (38) (1996) 9164.
[11] P. Wu, M. Iwamoto, J. Chem. Soc. Faraday Trans. 94 (1998) 2871.
[12] H. Kosslick, H. Landmesser, R. Frecke, J. Chem. Soc. Faraday Trans. 93 (9) (1997) 1849.
[13] N.S. Nesterenko, O.A. Ponomoreva, V.V. Yuschenko, I.I. Ivanova, F. Testa, F. Di Renzo, F. Fajula, Appl. Catal. A: Gen. 254 (2) (2003) 261.
[14] S. Udayakumar, S. Ajaikumar, A. Pandurangan, Appl. Catal. A: Gen. 307 (2) (2006) 245.
[15] G. Du, Y. Yang, W. Qiu, S. Lim, L. Pfefferle, G.L. Haller, Appl. Catal. A: Gen. 313 (1) (2006) 1.
[16] Y.-y. Huang, B.-y. Zhao, Y.-c. Xie, Appl. Catal. A: Gen. 172 (2) (1998) 327.
[17] M. Chidambaram, C. Venkatesan, A.P. Singh, Appl. Catal. A: Gen. 310 (2006) 79.
[18] S. Albertazzi, E. Rodríguez-Castellón, M. Livi, A. Jiménez-López, A. Vaccari, J. Catal. 228 (1) (2004) 218.
[19] M.L. Occelli, S. Biz, A. Auroux, Appl. Catal. A: Gen. 183 (2) (1999) 231.
[20] K. Chaudhari, R. Bal, T. Kr. Das, A. Chandwadkar, D. Srinivas, S. Sivasanker, J. Phys. Chem. B 104 (2000) 11066.
[21] E. Rodríguez-Castellón, A. Jiménez-López, P. Maireles-Torres, D.J. Jones, J. Rozière, M. Trombetta, G. Busca, M. Lenarda, L. Storaro, J. Solid State Chem. 175 (2) (2003) 159.
[22] Z.-G. Wu, Y.-X. Zhao, D.-S. Liu, Microporous Mesoporous Mater. 68 (2004) 27.
[23] A. Infantes-Molina, J. Mérida-Robles, P. Maireles-Torres, E. Finocchio, G. Busca, E. Rodríguez-Castellón, J.L.G. Fierro, A. Jiménez-López, Microporous Mesoporous Mater. 75 (2004) 23.
[24] X.X. Wang, L. Veyre, F. Lefebvre, J. Patarin, J.M. Basset, Microporous Mesoporous Mater. 66 (2003) 169.
[25] A. Tarafdar, A.B. Panda, P. Pramanik, Microporous Mesoporous Mater. 84 (2005) 223.
[26] P. Salas, L.F. Chen, J.A. Wang, H. Armendáriz, M.L. Guzman, J.A. Montoya, D.R. Acosta, Appl. Surf. Sci. 252 (4) (2005) 1123.
[27] E. Gianotti, E. Oliveira, V. Dellarocca, S. Coluccia, H.O. Pastore, L. Marchese, Stud. Surf. Sci. Catal. 141 (2002) 417.
[28] M.L. Peña, V. Dellarocca, F. Ray, A. Corma, S. Coluccia, Microporous Mesoporous Mater. 44–45 (2001) 345.
[29] E. Storino, J. Peri, R.J. Willcy, G. Basuca, J. Catal. 157 (1995) 57.
[30] A. Laachir, V. Perichon, A. Badri, J. Lamotte, E. Catherine, J.C. Lavalley, J. El Fallah, L. Hilarer, F. Le Normand, E. Uenere, G.N. Sauvion, O. Touret, J. Chem. Soc. Faraday Trans. 87 (1991) 1601.
[31] A.V. Ivanov, E. Zausa, Y. Ben Taârit, N. Essayem, Appl. Catal. A: Gen. 256 (2003) 225.
[32] J. Sun, M.-O. Coppens, Stud. Surf. Sci. Catal. 141 (2002) 85.
[33] D.J. Rosenberg, F. Coloma, J.A. Anderson, J. Catal. 210 (2002) 218.
[34] G. Engelhardt, D. Michel, High-Resolution Solid State NMR of Silicates and Zeolites, Wiley, New York, 1987.
[35] E. Fernández López, V. Sánchez Escribano, M. Panizza, M.M. Carnasciali, G. Busca, J. Mater. Chem. 11 (2001) 1891.
[36] S. Gontier, A. Tuel, Appl. Catal. A: Gen. 143 (1996) 125.
[37] T. López, J. Navarrete, R. Gómez, O. Novaro, F. Figueras, H. Armendariz, Appl. Catal. A: Gen. 125 (1995) 217.
[38] J.A. Anderson, C. Fergusson, I. Rodriguez-Ramos, A. Guerrero-Ruiz, J. Catal. 192 (2000) 344.
[39] M. Misono, N. Mizuno, K. Katamura, A. Kasai, Y. Konishi, K. Sakata, T. Okuhara, Y. Yoneda, Bull. Chem. Soc. Jpn. 55 (1982) 400.
[40] J. Haber, K. Pamin, L. Matachowski, D. Mucha, Appl. Catal. A: Gen. 256 (2003) 141.
[41] K. Nowinska, R. Fórmanial, W. Kaleta, A. Wącław, Appl. Catal. A: Gen. 256 (2003) 115.
[42] J.C. Edwards, C.Y. Thiel, B. Nenac, J.F. Knifton, Catal. Lett. 51 (1998) 77.
[43] V.M. Mastikhin, S.M. Kulikov, A.V. Nosov, I.V. Kozhevnikov, I.L. Mudrakovsky, M.N. Timofeeva, J. Mol. Catal. 60 (1990) 65.
[44] J.A. Wang, L.F. Chen, L. Noreña, J. Navarrete, J.L. Contreras, J. Catalysis (2007), in review.